PIV measurements over a double bladed Darrieus-type vertical axis wind turbine: a validation benchmark.

F. Arpino[1], G. Cortellessa[1], M. Scungio[2], G. Fresilli[1], A. Facci[2], A. Frattolillo[3]

[1]*Department of Civil and Mechanical Engineering, University of Cassino and Southern Lazio, Cassino (FR), Italy*
[2]*Department of Economics, Engineering, Society and Business Organization, University of Tuscia, Viterbo, Italy*
[3]*Department of Civil and Environmental Engineering and Architecture, University of Cagliari, Cagliari, Italy*

Abstract

Vertical axis wind turbines (VAWTs) are very attractive for in-home power generation since they can be adopted even at low wind speeds and highly variable wind direction. Even if significant experimental research activity has been carried out to improve VAWTs performance, the ability to accurately reproduce flow field characteristics around turbine blades by CFD (computational fluid dynamics) techniques represents a powerful approach to further enhance wind turbines performance. Thanks to CFD, in fact, it is possible to reproduce flow characteristics with a detail level impossible to achieve by experiments. Nevertheless, in order to appropriately analyze the flow structure by CFD application, an accurate validation is essential, and high-quality measurements of some main flow characteristics are required. In recent publications the authors investigated, both experimentally and numerically, the performance of an innovative double bladed Darrieus-type VAWT, with the aim to define an optimal configuration also focusing on self-starting ability of the prototype by employing CFD technique. Nevertheless, comparison between experiments and numerical results was made only in terms of power and torque coefficient. To overcome such limitation, in this paper the authors propose an experimental benchmark case for CFD results validation, describing detailed flow field in correspondence of one pair of blades of the innovative Darrieus-type VAWT in static conditions. Measurements were performed employing Particle Image Velocimetry (PIV) technique on a scaled model of the turbine blades realized by 3D printing. An uncertainty analysis was also performed which showed a high accuracy of the obtained experimental results. The measurements of the main flow characteristics (bi-dimensional velocity components) were then used for a test case CFD validation of two different turbulence models.

Keywords: *Vertical Axis Wind Turbine; Particle Image Velocimetry; CFD validation; Darrieus-style wind turbines; PIV uncertainty analysis*

1. INTRODUCTION

Wind turbines are mainly classified by means of their axis of rotation: Horizontal Axis Wind Turbines (HAWT) and Vertical Axis Wind Turbines (VAWT). VAWT, in respect to the HAWT, are able to

receive wind from different directions and allow to fix the generator at the bottom of the rotor and not on the tower. On the other hand, the turbulence phenomena over the blades are complex because the attack angle is variable with respect to the wind path [1]. Typical VAWT are represented by: i) the drag-based Savonius type, used mainly for small-scale power applications because of their low energy conversion efficiency [2]; ii) Darrieus type working on the basis of the lift forces acting on the blades, characterized by higher energy conversion efficiency but poor self-starting capability [3], that makes them particularly worth of investigation [4]. CFD (Computational Fluid Dynamics) represents a valuable support to experiments on wind turbines allowing significant times and costs reductions with respect to experiments [5]. Nevertheless, CFD numerical results if not validated can be affected by errors due to different factor, such as: representativeness of model geometry, definition of computational domain, choice of boundary conditions, employed turbulence modelling approach, etc. Therefore, a proper validation procedure is crucial to ensure fidelity and reliability of numerical predictions [6].

A significant amount of research activity was conducted in the last years for Darrieus type small-scale wind turbines in order to improve their performance. Singh et. al. [3] adopted CFD approach to study the self-starting ability of VAWT. In their analysis the conventional straight blades were replaced with unsymmetrical ones and, in this way, the rotor solidity was increased.

Zamani et. al. [7] performed numerical analysis by using the software OpenFOAM. They studied how a J-shaped profile of the blades, designed from a DU 06-W-200 aerofoil, can improve the starting torque. These numerical investigations showed that the J-shaped profile removes the pressure side of aerofoil from the maximum thickness toward the trailing edge.

Naccache et al. [8] proposed an optimization of the Darrieus-type VAWT extending the high-power generation area of the blades, by using a dual axis wind turbine.

J. Chen et al. [9] proposed a novel Darrieus turbine to improve the starting ability by using an opening. By CFD analysis the authors investigated the influence of the opening ratio and location on the performace of the Darrieus rotor. In addition, J. Chen et al. [10] conducted CFD investigation on the characteristics such as the power output. the static torque, vortex and pressure contours of a standard Darrieus rotor with two sets of blades. The effect of the distance between the outer and inner blades on the performance of the rotor was analysed.

Some of the authors of the present paper, in a previous research [11] analysed the performance of a real scale innovative configuration of Darrieus-type VAWT for small-scale power generation by means of 2D CFD investigations. The turbine was composed of three pairs of blades, each composed by a main and auxiliary aerofoil. The results of the simulations confirmed the capabilities of the investigated VAWT configuration to give valuable performance even for wind speeds below 4 $m \cdot$

s^{-1}. Besides, CFD investigations were used to assess self-starting ability of the innovative configuration of Darrieus-type VAWT by evaluating the torque generated by the rotor in static conditions (Static Torque, ST) [11] for different azimuth angles. Nevertheless, the numerical results were validated only in terms of bulk power and torque coefficients collected during wind tunnel experiments conducted at the University of Cassino and Southern Lazio, and it was observed that simulations and measurements were not compatible for very high Tip Speed Ration (TSR) [11], evidencing that a results validation in terms of local velocity field is actually required.

In the present paper, measurements performed on a pair of the VAWT blades investigated in [11] by employing the Particle Image Velocimetry (PIV) technique are presented. Measurements are used to realize a detailed benchmark case for CFD results validation in terms of local air velocity distribution in correspondence of the aerofoils surface. This represents the main novelty of the present papers since, according to the knowledge of the authors, a benchmark of VAWT composed by a pair of blades is proposed here for the first time.

In the last decades, PIV technique was adopted to produce quantitative flow velocity data for the validation of numerical simulations [12]–[14]. In particular, Castelein [15] realized a benchmark of VAWT in dynamic stall. Edwards [16] realized PIV measurements and CFD simulation of the performance and flow physics of a small-scale VAWT. In his analysis, Edwards found significant CFD-PIV differences in predicting flow re-attachment. In particular, at a higher tip speed ratio, the flow separates slightly later than in the previous condition. The wake structure behind a vertical axis wind turbine (VAWT) was both measured in a wind tunnel using PIV and computed with large-eddy simulation (LES) by Posa [17]. The dependence of the wake structure on the Tip Speed Ratio (TSR) was investigated, showing higher asymmetry and larger vortices at the lower rotational speed, due to stronger dynamic stall phenomena. Lam [18] studied the wake characteristics of a vertical axis wind turbine by two- and three-dimensional computational fluid dynamics simulations. The wake velocity field and turbulence field from 1 to 10 turbine diameters (1D to 10D) downstream were examined. Both the transition Shear Stress Transport (SST) and the Detached Eddy Simulation (DES) models were used to close the unsteady Reynolds-averaged Navier-Stokes (URANS) equations. The CFD models were validated by PIV test results from the literature. The regions of the near and far wakes were defined based on the occurrence of the maximum velocity deficit. In the near wake (within 3D), the velocity suffered a drastic deficit of about 85%. In the far wake (beyond 3D), major velocity recovery occurred with the average stream-wise velocity reaching approximately 75% at 10D.

In this paper, the authors propose measurements made out by PIV technique of main flow characteristics around a pair of airfoils of ~~a~~ the Darrieus-type VAWT already investigated in [11] and [19] in order to provide accurate and reliable data for CFD models validation. In particular, the

experimental bi-dimensional velocity fields were obtained in correspondence of the airfoils in static conditions (absence of blade rotation). An uncertainty analysis was also performed which showed a high accuracy of the obtained experimental results.

Such measurements (bi-dimensional velocity components) were then used for a test case of CFD model validation using two different RANS (Reynolds averaged Navier-Stokes) turbulence models, i.e. SST k-ω and Spalart-Allmaras, in order to verify their suitability in such validation procedures.

2. METHODS

In this section the experimental analysis by PIV technique on ~~a~~ one pair of not-rotating blades of the innovative Darrieus-type VAWT [11, 19] under investigation is illustrated.

2.1 Darrieus-type VAWT prototipe

In this paper the authors propose a benchmark for CFD validation by PIV technique on ~~the~~ a pair of not-rotating blades of an innovative VAWT configuration, investigated in previous works [11], [19] finalized to the definition of the optimal geometrical parameters maximizing torque and power coefficients.

The analysed VAWT is composed of three pairs of blades placed at 120° each other. Experimental and numerical analysis proposed in this paper were performed on ~~a~~ one pair of not-rotating blades composed by a main and an auxiliary aerofoil, as illustrated in Figure 1. The blades consists in a modified version of the DU 06-W-200 aerofoil available in the scientific literature [20].

PIV measurements were conducted on a 1:4 scale model realized with a 3D printer based on the "Fused Deposition Modelling" (FDM). In particular, the main aerofoil chord length, C_1, is equal to 68 mm and the ratio between main and auxiliary aerofoils chord lengths, C_2/C_1, is equal to 0.60, the angles of attack, α_1 and α_2, (the angles between the profile chord and the tangential velocity vector) are both fixed and equal to 12.5°; the distance between the two aerofoils, y, is equal to 18.40 mm, the longitudinal distance between the aerofoils, x, is equal to 25 mm., while the diameter and the height of the micro turbine model are equal to 120 mm and 140 mm respectively. Details about the investigated geometry are available in [19].

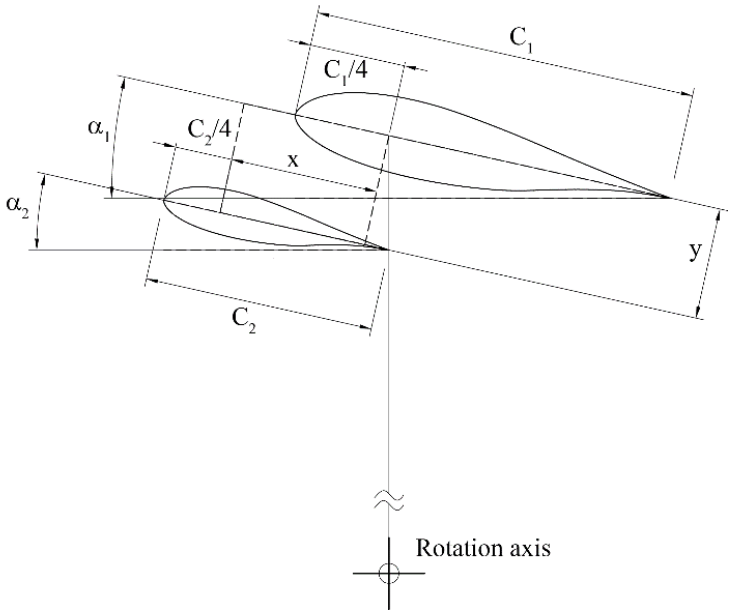

Figure 1. Geometrical configuration of the pair of blades investigated by PIV analysis.

2.2 Wind tunnel and PIV system setup

The wind tunnel of the Laboratory of Industrial Measurements (LaMI) of the University of Cassino and Southern Lazio (Italy) was employed to perform experimental analysis on the pair of blades. The apparatus is located in a 150 m^3 room equipped with a mechanical ventilation system with an air exchange rate of 0.3 h^{-1}. In this way it is possible to get constant humidity and temperature values equal to 20 ± 2 °C and 50 ± 5% RH, respectively. A schematic of the equipment is available in Figure 2. The wind tunnel of LaMI consists of the following components: an inlet nozzle (16:1 contraction ratio), flow conditioners (honeycombs), vortex generators, a flow establishment section, a test section, anti-swirl devices (honeycombs and grids) and a squirrel-cage centrifugal fan. The wind in the tunnel can reach a speed equal to 25 m/s by a DC motor equipped with a thyristor type control system. The wind tunnel manufacturer guarantees an expanded uncertainty, associated with air velocity measurements equal to 1.8% in the speed range 5÷20 m/s. In addition, the uniformity of the wind speed throughout the flow section was assessed by in-depth measurements of wind speed with a pitot tube on 13 evenly distributed points. From these analyses it was found that the maximum variation of the wind speed with respect to the centre of the flow section was <1% within an inner section of 20 cm of diameter, ensuring a good uniformity of the incoming flow on the VAWT under examination. Finally, the test chamber is of an Eiffel-type, with 1.1 m of height and 1.0 m of width. The wind tunnel of the LaMI is equipped with a Particle Image Velocimetry (PIV) measurement system, that allows 2D measurements of the air velocity field on a parallel plane with respect to the

air flow direction, according to the laser light that illuminates the measurement area from the top of the test chamber, as reported in Figure 2.

The physical principle on which the PIV technique is based is the following: in a short period of time the laser light illuminates twice the flow seeded by micron-sized particles. The illuminated particles allow to obtain two distinct images and by a cross-correlation method the local velocity vectors are reconstructed [21]. The PIV analysis allows to get the instantaneous velocity field in 2D dimensions because the time interval is short compared to the flow time scales [22]. Details about such non-intrusive measurement technique are available in the scientific literature [23], [24] and are not reported here for brevity.

The Laser of the PIV system is a NANO L135-15 while the camera is a TSI PowerView Plus model 7002262 equipped with 50 mm - 1:1.8 Nikkor optics.

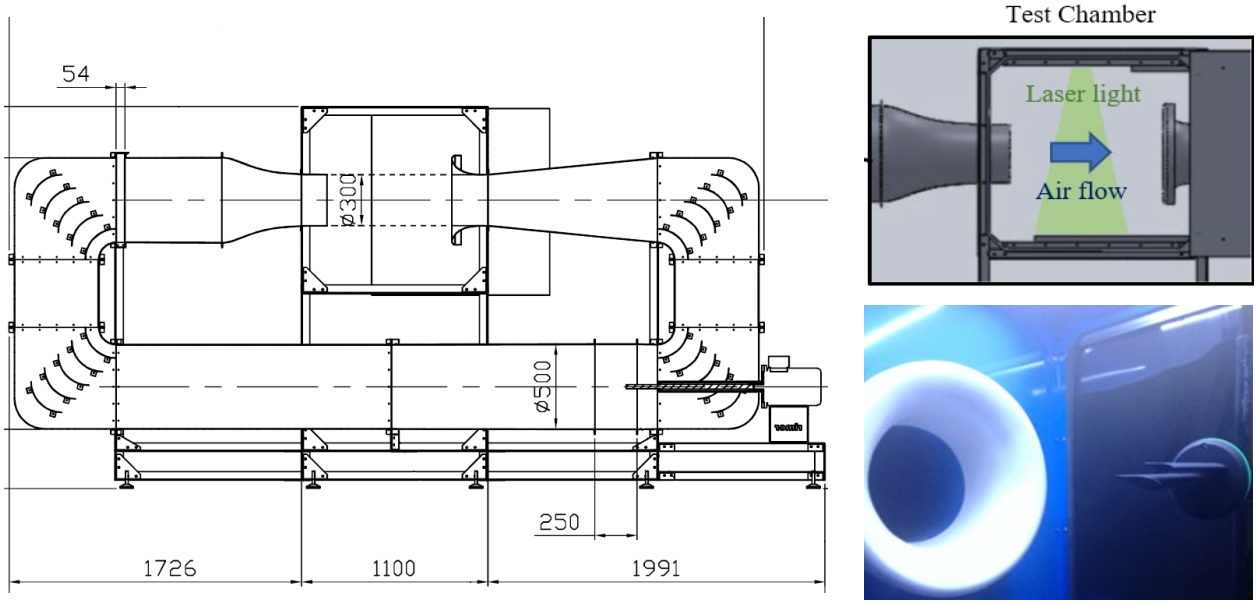

Figure 2. Wind tunnel available at the Laboratory of Industrial Measurements (LaMI).

2.3 Uncertainty analysis of the PIV measurements

The uncertainty analysis associated to the experimental data obtained by PIV system are based on the uncertainty propagation law [25], [26], [27]. A brief description of the procedure is reported below.

The principle of the PIV measurement can be described by the following equation [28]:

$$w = \alpha \frac{\Delta x}{\Delta t} + \delta w \tag{1}$$

where w is the velocity (m/s), Δx represents the pixel displacement of particles between PIV image pairs, δw (m/s) takes into account particle velocity lag from fluid acceleration together with three-

dimensional effects on prospective of the velocity field, and α (m/pixel) is the scaling magnification factor. The uncertainty associated to the PIV average velocity measurements can be evaluated by Equation 2:

$$u_w = \sqrt{u_A^2 + \left(\frac{\partial w}{\partial \alpha}\right)^2 u_\alpha^2 + \left[\frac{\partial w}{\partial(\Delta x)}\right]^2 u_{\Delta x}^2 + \left[\frac{\partial w}{\partial(\Delta x)}\right]^2 u_{\Delta t}^2 + u_{\delta w}^2} \quad (2)$$

where u_w is the measured velocity standard uncertainty, u_A is the type A uncertainty, that for the case under investigation was evaluated to be negligible with respect to other uncertainty contributions, while u_α, $u_{\Delta x}$, $u_{\Delta t}$, $u_{\delta w}$ represent the standard uncertainties of different influence parameters. In particular, the magnification factor is defined as:

$$\alpha = \frac{l_r \cos(\vartheta)}{L_r} \simeq \frac{l_r(1 - \frac{\vartheta^2}{2})}{L_R} \quad (3)$$

where l_r is the distance of the reference point expressed in mm, L_r is the distance of reference image expressed in pixel, ϑ is the prospective angle. The standard uncertainty of the magnification factor was evaluated by means of the following propagation law:

$$u_a = \sqrt{\left(\frac{\partial \alpha}{\partial L_R}\right)^2 \left({u_{L_R}}^2 + {u_{l_t}}^2\right) + \left(\frac{\partial \alpha}{\partial l_r}\right)^2 {u_{l_r}}^2 + \left(\frac{\partial \alpha}{\partial \vartheta}\right)^2 {u_\vartheta}^2 + \left(\frac{\partial \alpha}{\partial \theta_0}\right)^2 {u_{\theta_0}}^2} \quad (4)$$

where u_{lt} represents the standard uncertainty of the distance from target l_t, u_{lr} and u_{Lr} were evaluated as the ratio between the resolution (in meters and pixels, respectively) and $\sqrt{3}$, resulting in: $u_{l_r} = \frac{0.001}{\sqrt{3}}\ m$ and $u_{L_r} = \frac{1}{\sqrt{3}}\ pixel$. Similarly, the value of $u_{\Delta x}$ was evaluated as the ratio between the maximum error in the evaluation of x-displacement and $\sqrt{3}$, resulting in:

$$u_{\Delta x} = \frac{\left(d_p\ 1.2 \times 10^{-6}\right)}{\sqrt{3}}\ m \quad (5)$$

where the maximum error is evaluated as the mean diameter of the particles d_p $(1.2 \times 10^{-6}\ m)$. Finally, $u_{\Delta x}$ was considered to be negligible with respect to the other uncertainty contributions. The 3D effects on the prospective of velocity were evaluated as indicated in the following:

$$u_{\delta w} = 0.03\ U_{REF} \cdot \tan(\vartheta) \quad (6)$$

where U_{REF} is the uniform flow speed and ϑ is the prospective angle.

3. RESULTS

3.1 Experimental results

Since laser light that illuminates the prototype for PIV measurements comes from the top of the wind tunnel test chamber and no measurement is possible in shadowed areas, two tests have been realized:

the Test 1 has been realized adopting the geometrical configuration illustrated in Figure 1, while the Test 2 has been realized by mirroring the 1:4 scale turbine prototype with respect to horizontal plane. Test 1 and Test 2 were performed at the same air velocity and at the same position in the test chamber of the wind tunnel. Therefore, Test 1 allowed to measure the velocity field only on the top of the prototype, while Test 2 allowed measurements on the bottom side. In Table 1, the configuration parameters selected for the two tests are listed.

In Figure 3, the blades image taken in the wind tunnel are reported. In particular, fog particles and instantaneous velocity vectors reconstruction during Test 1 (measurement from the top) are illustrated in Figure 3(a) and Figure 3(b) respectively, while fog particles and instantaneous velocity vectors reconstruction during Test 2 (measurement from the bottom) are illustrated in Figure 3(c) and Figure 3(d), respectively.

Table 1. PIV configuration parameters

Step	**Description**	**PIV Test 1 illumination from the top**	**PIV Test 2 illumination from the bottom**
Calibration	Object distance from millimetres to pixels	14.01 px/mm	14.01 px/mm
Lens distance	The physical distance between the camera lens and the section illuminated by the laser	58.5 cm	58.5 cm
Engine power	Percentage of the wind tunnel engine – wind velocity	28% - 10 m/s	28% - 10 m/s
Lens opening	Size of the lens aperture	4	4
Laser A energy	Energy emitted by the laser during the frame A acquisition	800mJ	700 mJ
Laser B energy	Energy emitted by the laser during the frame B acquisition	820mJ	780 mJ
Frequency	Acquisition frequency of the photographs	7.25 Hz	7.25 Hz
Time	Time interval between the frame A and frame B capture	0.00000021 s	0.00000021 s
Interrogation cell	Interrogation cell dimensions	from 16x16 to 32x32	from 16x16 to 32x32

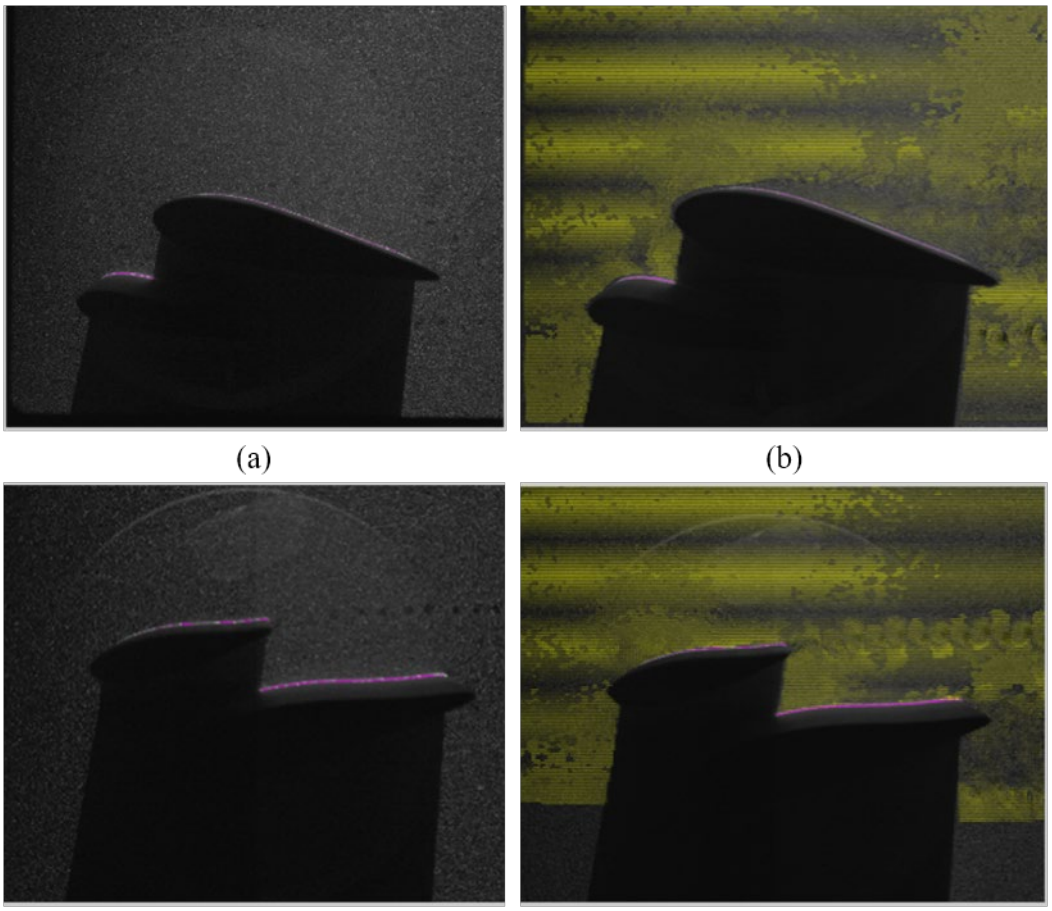

Figure 3. Image of the blades taken in the wind tunnel. Fog particles (a) and velocity vectors reconstruction (b) during Test 1; fog particles (c) and velocity vectors reconstruction (d) during Test 2.

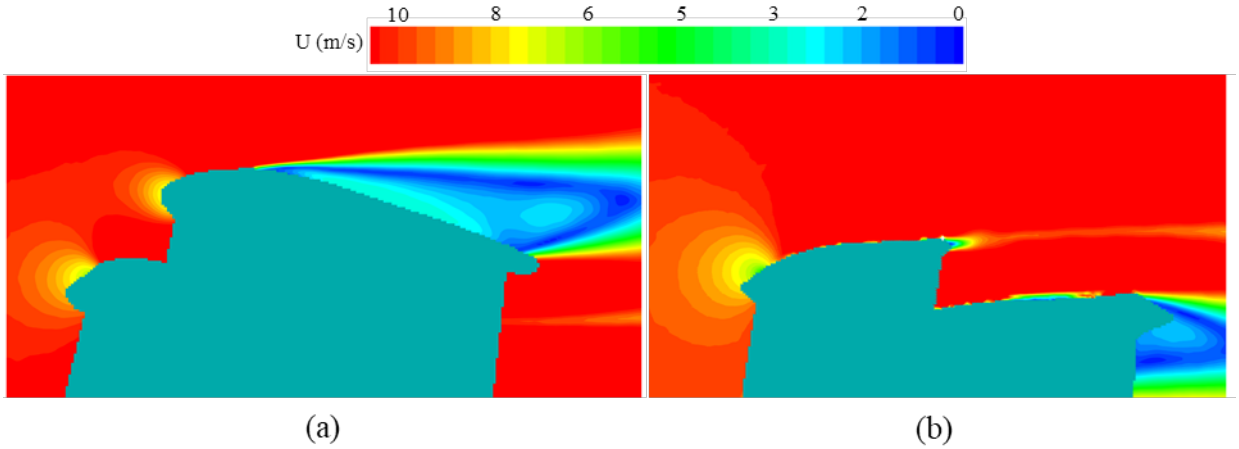

Figure 4. Experimental averaged velocity (m/s) fields for Test 1 (a) and for Test 2 (b).

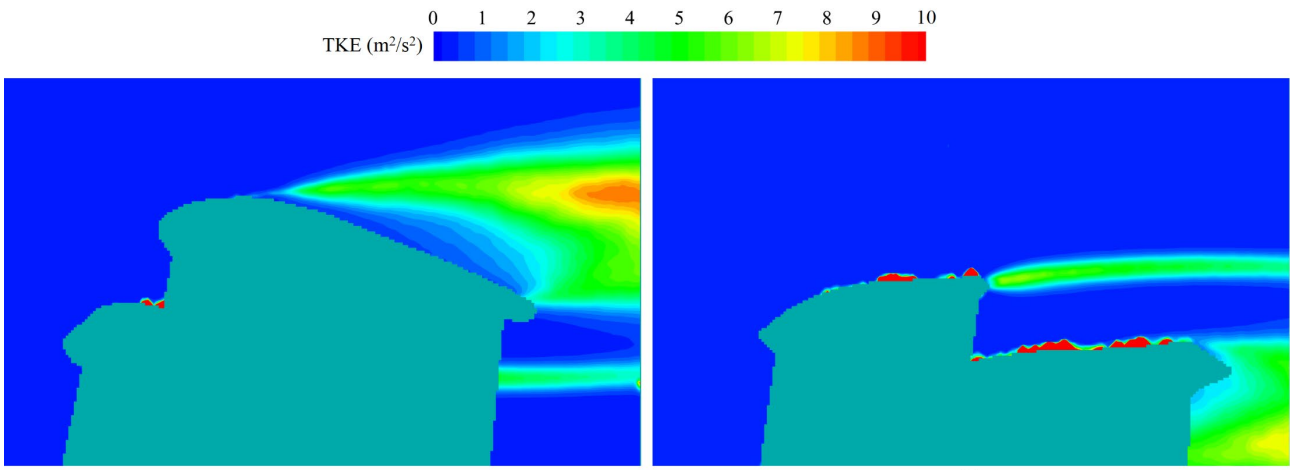

Figure 5. Experimental averaged TKE fields (m^2/s^2) for Test 1 (a) and for Test 2 (b).

The averaged velocity contours, obtained by averaging 1500 PIV instantaneous measurements are reported in Figure 4(a) and Figure 4(b) for Test 1 and Test 2, respectively. From the figure it is possible to observe a distortion of the flow lines and a vortex shedding phenomenon at the leading edge of the auxiliary blade.

For the angle of attack investigated a flow separation is observed for the main blade, with a much thicker wake zone with respect to the auxiliary blade. As expected, the maximum TKE is observed in the main blade wake region, reaching about double of the auxiliary blade wake region value. In the case of auxiliary blade, no significant flow separation is observed and the position of the stagnation point is shifted of about $0.07C_2$ in the direction of the upper surface with respect to the leading edge. In addition, in Figure 5(a) and Figure 5(b), the turbulent kinetic energy (TKE) contours are reported for Test 1 and Test 2, respectively. As expected, the highest TKE values were observed in the wake of both main and auxiliary blades, with some peak values in correspondence of the lower surface of both the airfoils, as highlighted for Test 2 in Figure 5(b).

3.2 Statistical convergence

In order to evaluate the required number of acquisitions for the statistical convergence, a convergence analysis was performed in correspondence of sections P1, P2 and P3 for both Test 1 and Test 2 (see Table 7). In particular, 250 instantaneous velocity acquisitions have been added for the calculation of the averaged fields at each step of the sensitivity analysis, until the percentage deviation was observed to be below 1% between two successive steps.

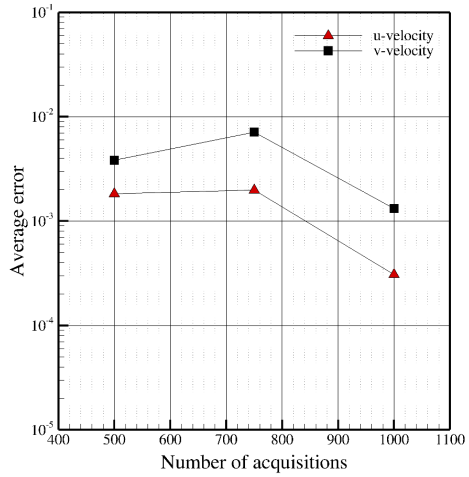

(a)

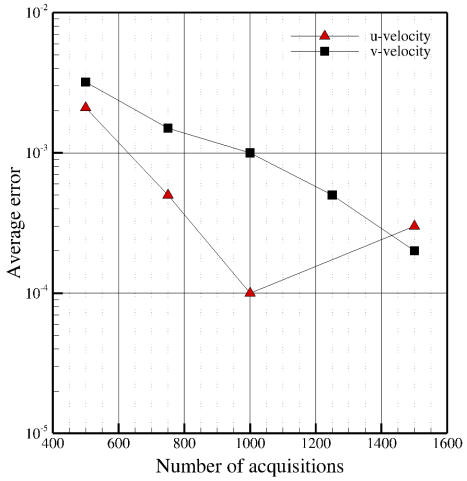

(b)

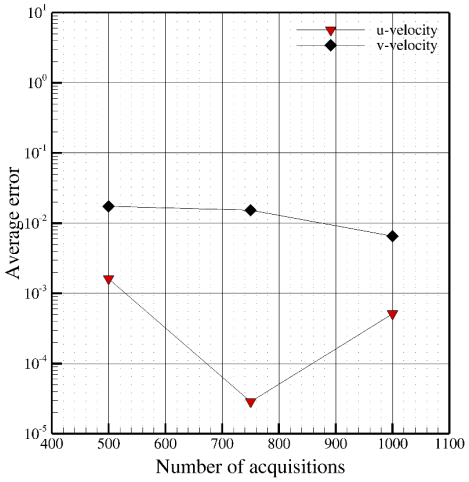

(c)

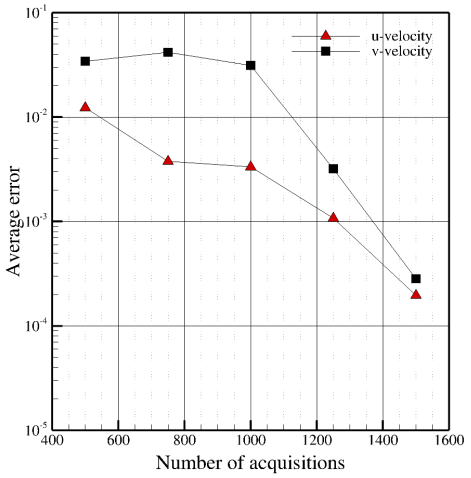

(d)

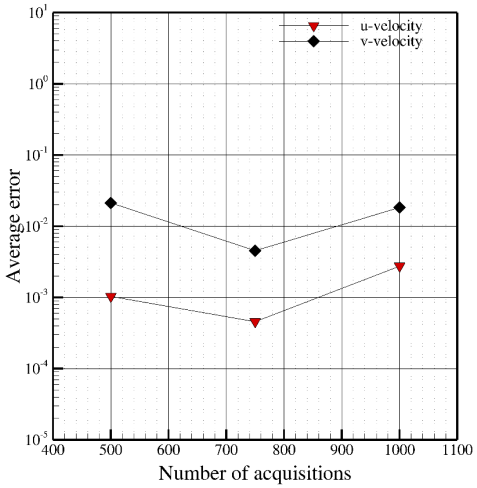

(e)

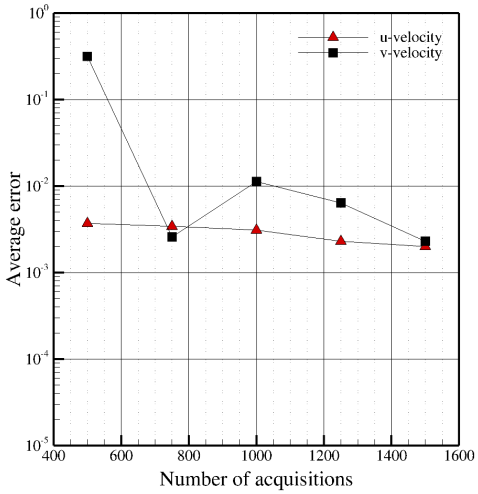

(f)

Figure 6. Results of the statistic convergence. Average error as a function of the number of acquisitions obtained in correspondence of the profile P1 for Test 1 (a) and Test 2 (b), in correspondence of the profile P2 for Test 1 (c) and Test 2 (d), in correspondence of the profile P3 for Test 1 (e) and Test 2 (f).

In Figure 6 the results of the statistic convergence are illustrated in terms of u-velocity and v-velocity average errors as a function of the acquisitions number. From the analysis of obtained results it derives that an acquisition number equal to 1000 was sufficient to get an error below 1% (Figure 6a, Figure 6c and Figure 6e) ensuring the statistic convergence for Test 1, while for Test 2 an acquisition number of 1500 images was necessary in order to limit the error (Figure 6b, Figure 6d, Figure 6f) not larger than 1%.

3.3 Uncertainty analysis results

In order to perform the uncertainty analysis, it is necessary to evaluate the relative standard uncertainty of all the contributions. The input parameters necessary to perform PIV measurements are listed in Table 2.

Table 2. Input parameters used for PIV measurements

Parameter	**Test 1**	**Test 2**
Measurement area (square) (m)	0.12	0.13
Uniform flow speed (m/s)	9.72	9.72
Magnification factor, alfa (m/px)	7.11E-05	7.11E-05
Distance of reference points, lr (m)	0.12	0.13
Distance of reference image, Lr (px)	1688	1828
Time interval (s)	0.000021	0.000021
Distance from target, lt (m)	0.585	0.585
Camera resolution (px)	2048	2048
Sampling frequence (Hz)	7.25	7.25
Particles average diameter (m)	1.20E-06	1.20E-06
Correlazion area size (px)	16	16

The results of the standard uncertainty contributions for Test 1 are listed in Table 3.

Table 3. Standard uncertainty of the calibration factors

	Uncertainty source	Parameter	Sensitivity coefficient	Standard uncertainty
Calibration board	Distance of reference image	L_r	$\frac{\partial \alpha}{\partial L_r} = -\frac{l_r}{{L_r}^2} = -4.21x10^{-8}\frac{m}{px^2}$	$u_{L_r} = \frac{1}{\sqrt{3}} = 5.77x10^{-1}\ px$
	Distance of reference points	l_r	$\frac{\partial \alpha}{\partial l_r} = \frac{1}{{l_r}^2} = 5.92x10^{-4}\frac{1}{px}$	$u_{l_r} = \frac{1.00x10^{-3}}{\sqrt{3}} = 5.77x10^{-4}\ px$
Optical system	Image distortion	$0.5\%\ L_r$	$\frac{\partial \alpha}{\partial L_r} = -\frac{l_r}{{L_r}^2} = -4.21x10^{-8}\frac{m}{px^2}$	$u_{Dis} = \frac{0.005xL_r}{\sqrt{3}} = 4.87px$
Experimental condition	Reference board position	l_t	$\frac{\partial \alpha}{\partial l_t} = \frac{l_r}{l_t L_r} = 1.22x10^{-4}\frac{1}{px}$	$u_{l_t} = \frac{5.00x10^{-3}}{\sqrt{3}} = 5.77x10^{-3}\ m$
	Parallel reference board	ϑ	$\frac{\partial \alpha}{\partial \vartheta} = -\frac{l_r \vartheta}{L_r} = -2.48x10^{-6}\frac{m}{px}$	$u_\vartheta = \frac{2\cdot\pi}{180\sqrt{3}} = 0.020\ rad$
Image detection	Normal vie angle	θ_0	$\frac{\partial \alpha}{\partial \theta_0} = -\frac{l_r \theta_0}{L_r} = -2.48x10^{-6}\frac{m}{px}$	$u_{u_{\vartheta_0}} = \frac{2\cdot\pi}{180\sqrt{3}} = 0.020\ rad$

The standard uncertainty of the scaling magnification factor (u_a) evaluated by means of Equation (7) is equal to $8.11\ x10^{-7}$m/px. Then, the evaluation of the remaining sensitivity coefficients with the relative standard uncertainties was performed, as shown in Table 4.

Table 4. Contributions for the composed velocity uncertainty calculation for Test 1

	Uncertainty source	Standard uncertainty	Sensitivity coefficient	Standard uncertainty
	Type A uncertainty	u_A	-	0.1 m/s
Velocity sensitivity coefficients	Scaling magnification factor	u_a	$\frac{\partial u}{\partial \alpha} = 1.37x10^5 \frac{\text{px}}{\text{s}}$	$8.11\ x10^{-7}$ m/px
	Displacement of particle image	$u_{\Delta x}$	$\frac{\partial u}{\partial(\Delta x)} = \frac{\alpha}{\Delta t} = 3.39 \frac{m\ px}{s}$	$9.75\ x10^{-3}$ px
	Time interval	$u_{\Delta t}$	$\frac{\partial u}{\partial(\Delta t)} = \frac{\partial u}{\partial(\delta u)} = 1\ s$	0.000021 s
Particle Trajectory	3D effects on prospective of velocity	$u_{\delta w}$	-	0.074 m/s

Finally, as a result of the uncertainty analysis for Test 1, it was found that the expanded velocity uncertainty, calculated by Equation (8), assuming a coverage factor k=2 (confidence level 95%), was equal to 0.17 m/s. Similarly, the results of the standard uncertainty contributions for Test 2 are listed in Table 5.

Table 5. Standard uncertainty of the calibration factors

	Uncertainty source	Parameter	Sensitivity coefficient	Standard uncertainty
Calibration board	Distance of reference image	L_r	$\frac{\partial \alpha}{\partial L_r} = -\frac{l_r}{{L_r}^2} = -3.89x10^{-8} \frac{m}{px^2}$	$u_{L_r} = \frac{1}{\sqrt{3}} = 5.77x10^{-1}\ px$
	Distance of reference points	l_r	$\frac{\partial \alpha}{\partial l_r} = \frac{1}{{l_r}^2} = 5.47x10^{-4} \frac{1}{px}$	$u_{l_r} = \frac{1.00x10^{-3}}{\sqrt{3}} = 5.77x10^{-4}\ px$
Optical system	Image distortion	$0.5\%\ L_r$	$\frac{\partial \alpha}{\partial L_r} = -\frac{l_r}{{L_r}^2} = -3.89x10^{-8} \frac{m}{px^2}$	$u_{Dis} = \frac{0.005xL_r}{\sqrt{3}} = 5.28px$
Experimental condition	Reference board position	l_t	$\frac{\partial \alpha}{\partial l_t} = \frac{l_r}{l_t L_r} = 1.22x10^{-4} \frac{1}{px}$	$u_{l_t} = \frac{5.00x10^{-3}}{\sqrt{3}} = 5.77x10^{-3}\ m$
	Parallel reference board	ϑ	$\frac{\partial \alpha}{\partial \vartheta} = -\frac{l_r \vartheta}{L_r} = -2.48x10^{-6} \frac{m}{px}$	$u_\vartheta = \frac{2 \cdot \pi}{180\sqrt{3}} = 0.020\ rad$
Image detection	Normal vie angle	θ_0	$\frac{\partial \alpha}{\partial \theta_0} = -\frac{l_r \theta_0}{L_r} = -2.48x10^{-6} \frac{m}{px}$	$u_{u_{\vartheta_0}} = \frac{2 \cdot \pi}{180\sqrt{3}} = 0.020\ rad$

The standard uncertainty of the scaling magnification factor, evaluated by means of Equation (9) for Test 2 is equal to $8.00\ x10^{-7}$m/px. Then, the evaluation of the remaining sensitivity coefficients

with the relative standard uncertainties was performed, as shown in Table 6. Finally, as a result of the uncertainty analysis for Test 2, it was found that the composed velocity uncertainty, calculated by Equation (10) assuming a coverage factor k=2 (confidence level 95%), was equal to 0.17 m/s.

Table 6. Contributions for the composed velocity uncertainty calculation for Test 2

	Uncertainty source	Standard uncertainty	Sensitivity coefficient	Standard uncertainty
	Type A uncertainty	u_A	-	0.1 m/s
Velocity sensitivity coefficients	Scaling magnification factor	u_a	$\frac{\partial u}{\partial \alpha} = 1.37x10^5 \frac{\text{px}}{\text{s}}$	8.00 $x10^{-7}$ m/px
	Displacement of particle image	$u_{\Delta x}$	$\frac{\partial u}{\partial(\Delta x)} = \frac{\alpha}{\Delta t} = 3.39 \frac{m\ px}{s}$	9.74 $x10^{-3}$ px
	Time interval	$u_{\Delta t}$	$\frac{\partial u}{\partial(\Delta t)} = \frac{\partial u}{\partial(\delta u)} = 1\ s$	0.000021 s
Particle Trajectory	3D effects on prospective of velocity	$u_{\delta w}$	-	0.074 m/s

In addition, the u' field limited between 0.01 m/s and 0.04 m/s for both Test 1 and Test 2 is reported in Figure 7. From the analysis of that figure it is possible to observe that u' assumes the highest values in correspondence of the wake with some peak values in correspondence of the lower surface of both the airfoils,

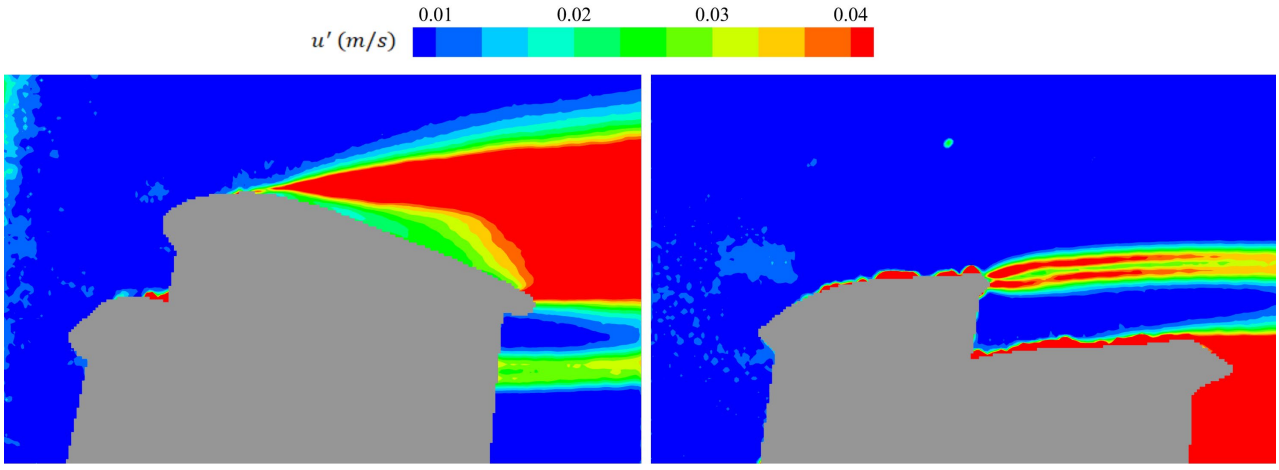

(a) (b)

Figure 7. u' fields as calculated for the PIV measured data obtained for Test 1 (a) and Test 2 (b).

3.4 The proposed benchmark case

On the basis of conducted measurements, in Figure 8 information about computational domain and the boundary conditions to be employed for numerical investigations are illustrated. The

computational domain has been realized on the basis of the wind tunnel characteristics, considering only the part of the stream flow with a good uniformity. The reference system is placed at the leading edge of the auxiliary blade, 300 mm from the inlet section.

At the inlet section, a constant and uniform x-component of the velocity equal to 10 m/s with a turbulence intensity equal to 0.5% reproduces the measured average velocity and turbulence intensity from PIV measurements. The distance between inlet section and auxiliary airfoil was set to 300 mm to reproduce model placement in the test chamber of the wind tunnel. On the basis of experimental observations, domain height was set to 340 mm, allowing the employment of symmetry boundary condition at the top and bottom sides of the domain. Given the order of magnitude of velocity, the fluid flow can be modelled as incompressible and a zero-pressure boundary condition is prescribed at the outlet section. Finally, no slip condition is adopted on solid blade surfaces. The whole computational domain is 340 mm height (equal to 5 times the chord lengths of the main blade) and 680 mm width (equal to 10 times the chord lengths of the main blade). Since the air temperature during experiments was kept at 20 ± 2 °C, the fluid can be assumed to be isotherm with constant and uniform thermophysical properties.

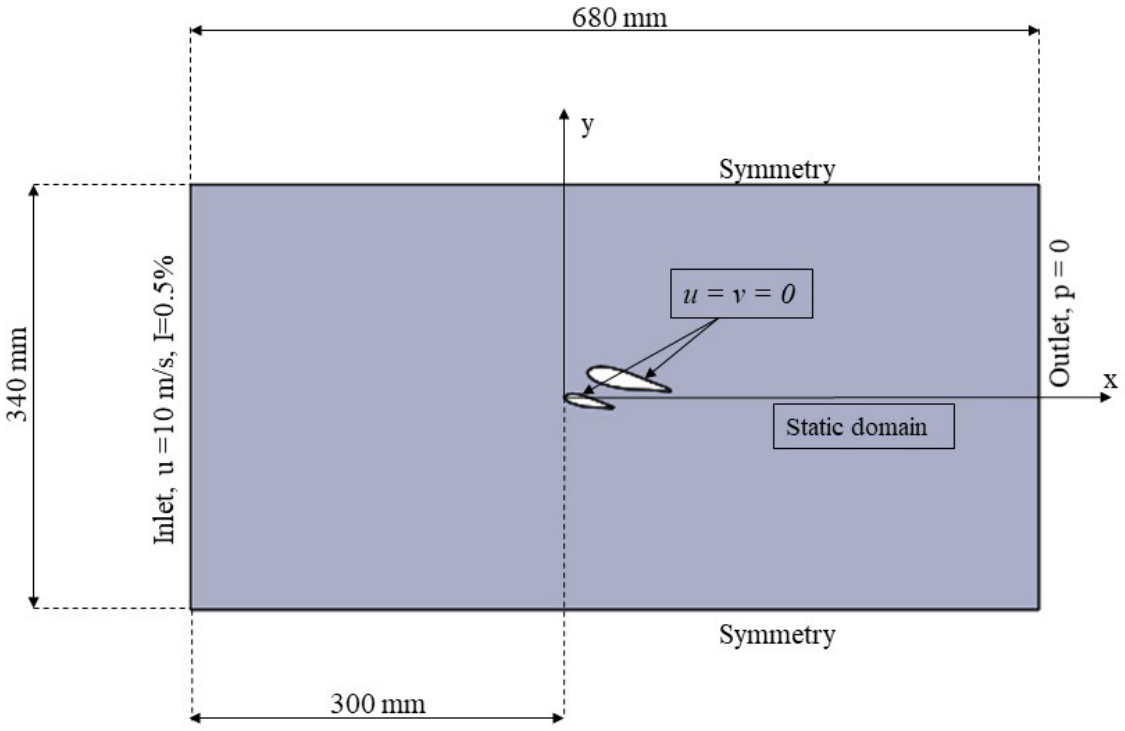

Figure 8. Computational domain and boundary conditions employed for the numerical simulations.

3.5 Mathematical and Numerical model: comparison with experiments

The numerical analysis was performed using the open source software OpenFOAM. The fluid flow impacting the pair of blades was investigated by solving the mass and momentum conservation

equations, and modelling the turbulence phenomena adopting an Unsteady Reynolds Averaged Navier-Stokes (URANS) model. Details about the employed partial differential equations are available in the scientific literature [11], [29] and are not reported here for brevity. On the basis of results presented in [11], two different turbulence models were employed for numerical investigations: the SST k-ω and the Spalart-Allmaras (S-A) turbulence models. Simulations were conducted in a bi-dimensional domain and in transient state, using a time step value equal to $1 \cdot 10^{-5} s$, and employing a second order discretization scheme for the upwind scheme. Simulations were performed employing the unstructured computational grid available in Figure 9, that is composed by 1709097 cells and ~~s~~ was chosen on the basis of a proper mesh sensitivity analysis. In order to reproduce the velocity field in the wake region and in correspondence of airfoils solid surfaces, the grid was refined in the wake region and near the walls, where a "viscous layer" was applied with a number of layers equal to 10, a minimum mesh size of $9x10^{-5}$ m and a growth rate of 1.1. The maximum computational grid size in the free stream is equal to 1.2 mm.

Numerical and PIV data are here compared and analyzed in order to provide a test case for the suitability of the PIV data in CFD model validation. The comparisons are shown in terms of horizontal (u) and vertical (v) components of the velocity in the four different vertical sections across the wind turbine airfoils indicated in Table 7 and schematically reported in Figure 10.

The Figure 11 and Figure 12 show the PIV data measured in the wind tunnel as well as the numerical results obtained with the SST k-ω and the Spalart-Allmaras (S-A) turbulence models. Error bars in the figures represent measurement uncertainty. On the basis of the velocity data reported in Figure 11 and Figure 12, the PIV measured data allow to observe that the SST k-ω turbulence model shows an overall better ability to reproduce the flow pattern around the airfoils if compared to the PIV measured data. In particular, looking at the u-velocity profiles on the upper surface of the main airfoil (Figure 11) it is clear that the S-A turbulence model is not able to reproduce the flow separation observed in the PIV measurements at the considered angle of attack (Figure 4). In fact, while both the turbulence models perform in a satisfying way as long as the fluid remains attached to the surface (upper sides of P1 and P2 in Figure 11), when the flow starts to separate, the S-A model fails to correctly visualize such separation, while the SST k-ω model is able to reproduce the recirculation zone due to such flow separation (upper sides of P3 and P4 in Figure 11). The measured PIV data allows also to observe a similar behaviour for the v-velocity component, with an overall better performance of the SST k-ω model, which is able at least to reproduce the shape of the experimental profiles where the S-A model largely fails, especially in the high separation zone of the main airfoil upper surface (upper sides of the v-velocity profiles P3 and P4, Figure 12).

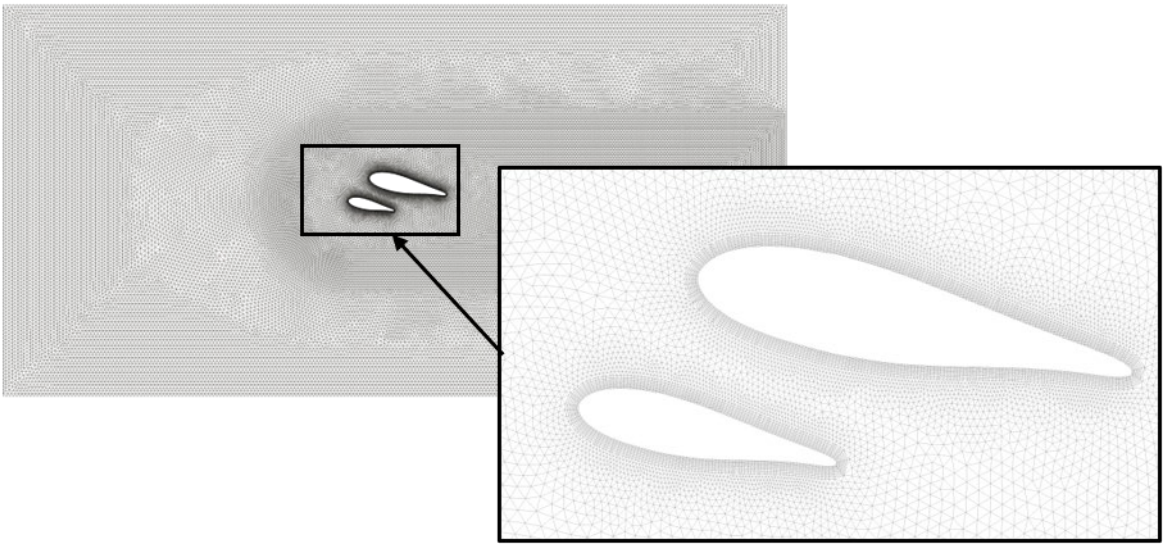

Figure 9. Computational grid composed by 1709097 cells.

Table 7. Geometric coordinates of the velocity profiles extracted along the blades.

Profile	x-coordinate (mm)	y-coordinate (mm)
Reference	0	from 40 to -40
P1	10	from 40 to -40
P2	30	from 40 to -40
P3	50	from 40 to -40
P4	70	from 40 to -40

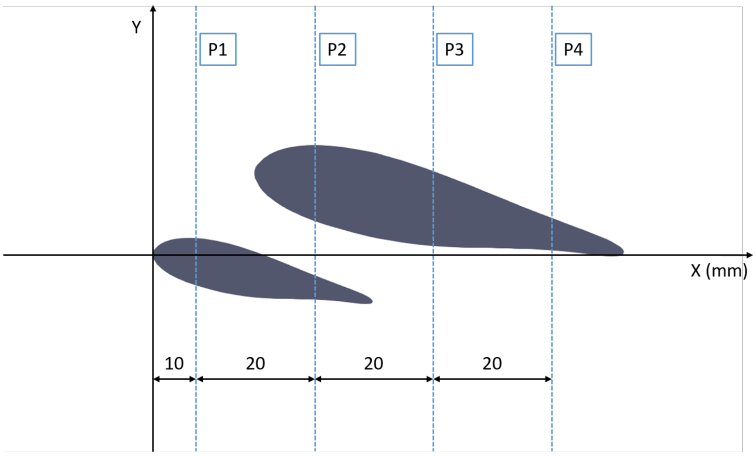

Figure 10. Different sections across the wind turbine blades in which the horizontal and vertical components of the velocity are compared with the PIV measurements.

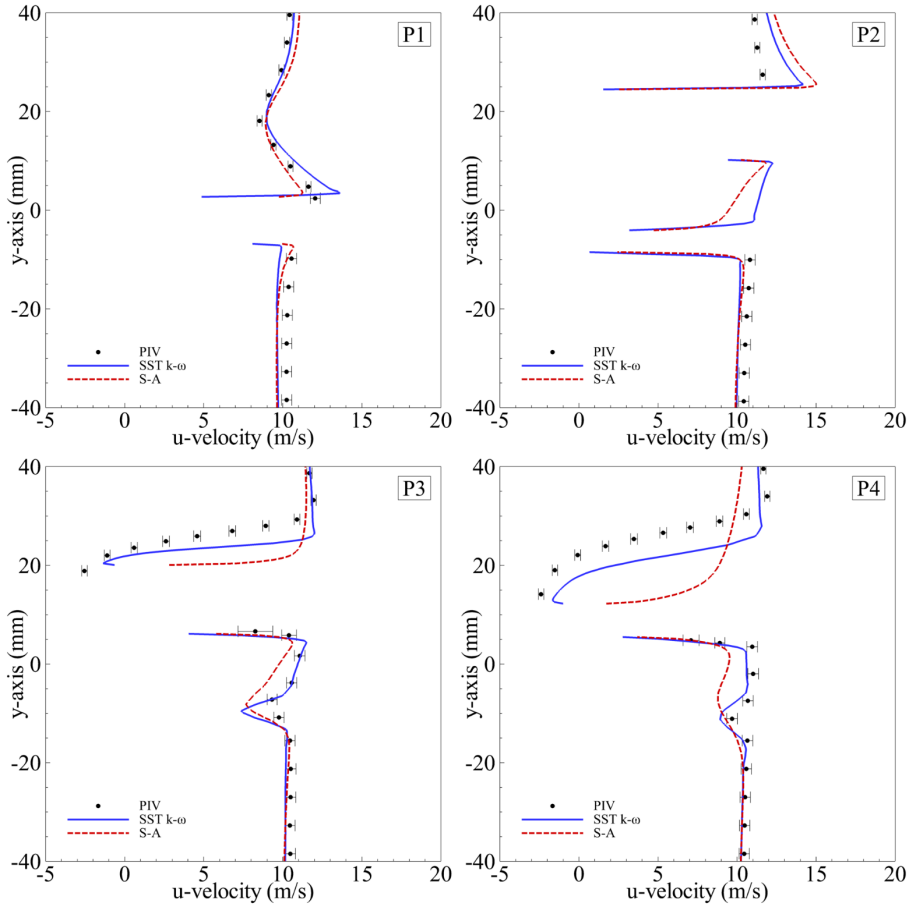

Figure 11. Comparison between CFD and PIV results in terms of horizontal component of the velocity (u) in different vertical sections across the wind turbine blades.

In terms of velocity field, a better agreement is observed between PIV and numerical data in the lower region of the analysed profiles with respect to the corresponding upper region. In this zone, in fact, the recirculation due to the separating flow is less pronounced and both the adopted numerical turbulence models give results that better fit the PIV data since no significant adverse gradient pressure is observed. This is confirmed by observing that the numerical results obtained from the SA turbulence model, that suffers the presence of adverse pressure gradient regions, are in bad agreement with PIV data in the separated flow region of the main blade (upper zone of the P4 profiles). In order to evaluate the ability of the turbulence model to correctly predict the flow field variables, in Figure 13 a comparison between PIV data and numerical data are reported in terms of turbulent kinetic energy (TKE), as predicted by the SST k-ω model.

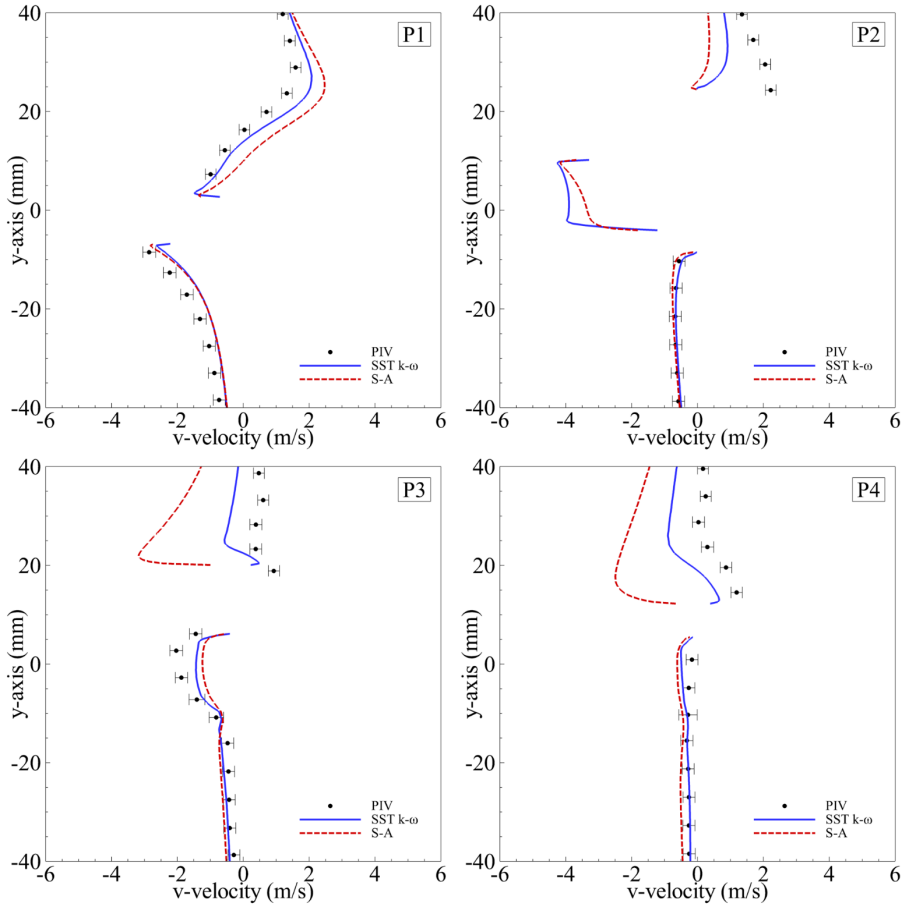

Figure 12. Comparison between CFD and PIV results in terms of vertical (along y) component of the velocity (u) in different vertical sections across the wind turbine blades.

From the analysis of Figure 13, it can be highlighted an overall good ability of the SST k-ω model to predict turbulent characteristics of the flow in the upper part of the domain (Test 1), while in the lower part (Test 2) the model performs worse, failing in predicting the magnitude of the TKE measured in the wake of the auxiliary airfoil (bottom panels of Figure 13, lower part of the profiles). In the upper region of the profiles (P3 and P4 sections) it can be seen that the numerical results are slightly shifted down along the y-axis with respect to PIV data even though the magnitude of the TKE is well reproduced. It should be pointed out, however, that for P1 and P2 sections there is a lack of PIV data due to the difficulty of made such measurements, and then a comprehensive comparison between numerical and experimental data is not possible.

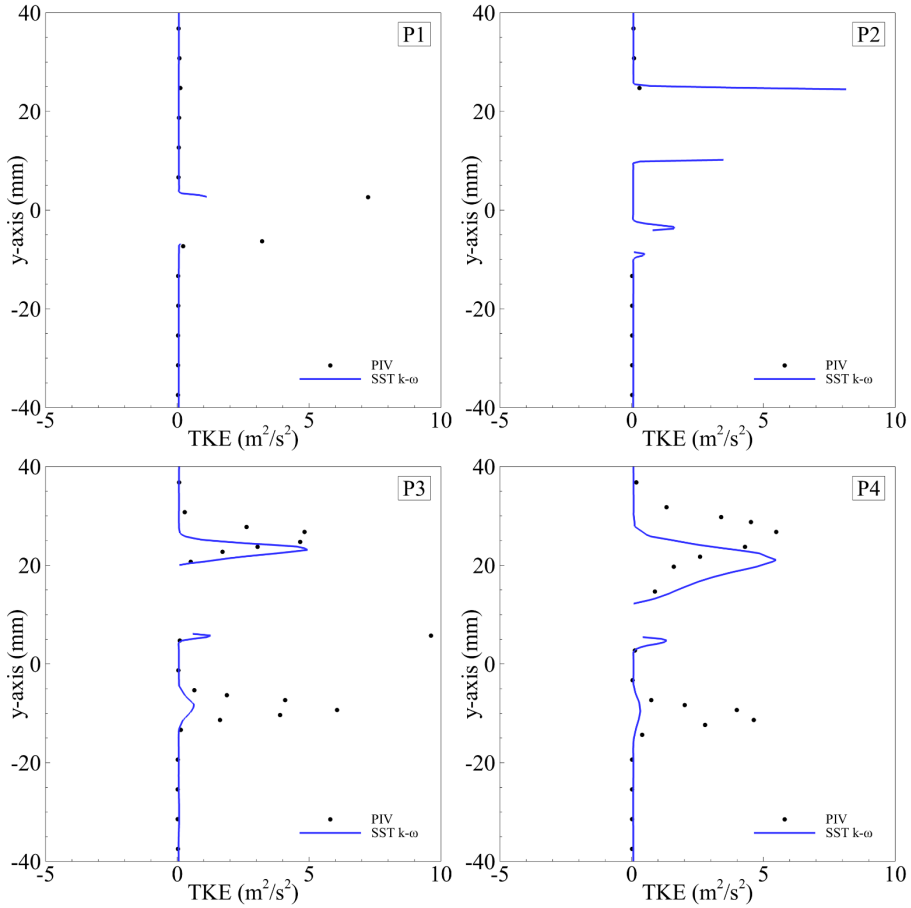

Figure 13. Comparison between CFD and PIV results in terms of vertical (along y) component of the turbulent kinetic energy (TKE) in different vertical sections across the wind turbine blades.

4. CONCLUSIONS

In this paper, the authors propose a validation benchmark for CFD models by providing accurate and reliable flow measurements made out by a PIV technique finalized to the determination of the velocity field around ~~a~~ one pair of static blades of an innovative Darrieus-style Vertical Axis Wind Turbine (VAWT) in static conditions (absence of blade rotation).

The analysed turbine configuration, already investigated both experimentally and numerically in our previous publications in terms of power and torque coefficients as well as in terms of self-starting ability, is composed of three couples of aerofoils (main and auxiliary) and, as reported in previous publications, has shown good capabilities to operate even for wind speeds below 4 $m \cdot s^{-1}$ (domestic applications). The PIV measurements were carried out on a 3D printed, scaled model of a pair of static blades adequately studied in a closed-circuit wind tunnel facility available in the Laboratory of Industrial Measurement (LaMI) of the University of Cassino and Lazio Meridionale. The experimental measurements were accurately carried out and the uncertainty associated to each flow variable was calculated based on the uncertainty propagation law. In order to verify the suitability of

the measured data to be used in a CFD model validation procedure, a CFD test case was carried out by using two different turbulence models.

From the proposed results it was shown that with the PIV measured flow field data, an accurate validation of the CFD model can be performed, a detailed analysis of the flow characteristics around the airfoils of the VAWT under investigation.

To the best of our knowledge at the time of writing, a CFD model validation tool for the specific VAWT configuration, i.e. composed by three couple of airfoils, is proposed for the first time in the scientific literature with the present paper.

5. REFERENCES

[1] Y. Bazilevs, A. Korobenko, X. Deng, J. Yan, M. Kinzel, e J. O. Dabiri, «Fluid-structure interaction modeling of vertical-axis wind turbines», *J Appl Mech Trans ASME*, vol. 81, n. 8, 2014, doi: 10.1115/1.4027466.

[2] J. V. Akwa, H. A. Vielmo, e A. P. Petry, «A review on the performance of Savonius wind turbines», *Renewable Sustainable Energy Rev*, vol. 16, n. 5, pagg. 3054–3064, 2012, doi: 10.1016/j.rser.2012.02.056.

[3] M. A. Singh, A. Biswas, e R. D. Misra, «Investigation of self-starting and high rotor solidity on the performance of a three S1210 blade H-type Darrieus rotor», *Renew. Energy*, vol. 76, pagg. 381–387, 2015, doi: 10.1016/j.renene.2014.11.027.

[4] A. R. Sengupta, A. Biswas, e R. Gupta, «Studies of some high solidity symmetrical and unsymmetrical blade H-Darrieus rotors with respect to starting characteristics, dynamic performances and flow physics in low wind streams», *Renew. Energy*, vol. 93, pagg. 536–547, 2016, doi: 10.1016/j.renene.2016.03.029.

[5] A. G. Malan, R. W. Lewis, e P. Nithiarasu, «An improved unsteady, unstructured, artificial compressibility, finite volume scheme for viscous incompressible flows: Part I. Theory and implementation», *Int. J. Numer. Methods Eng.*, vol. 54, n. 5, pagg. 695–714, 2002, doi: 10.1002/nme.447.

[6] C. J. Roy, «Review of code and solution verification procedures for computational simulation», *J. Comput. Phys.*, vol. 205, n. 1, pagg. 131–156, 2005, doi: 10.1016/j.jcp.2004.10.036.

[7] M. Zamani, M. J. Maghrebi, e S. R. Varedi, «Starting torque improvement using J-shaped straight-bladed Darrieus vertical axis wind turbine by means of numerical simulation», *Renew. Energy*, vol. 95, pagg. 109–126, 2016, doi: 10.1016/j.renene.2016.03.069.

[8] G. Naccache e M. Paraschivoiu, «Development of the Dual Vertical Axis Wind Turbine Using Computational Fluid Dynamics», *J Fluids Eng Trans ASME*, vol. 139, n. 12, 2017, doi: 10.1115/1.4037490.

[9] J. Chen, H. Yang, M. Yang, e H. Xu, «The effect of the opening ratio and location on the performance of a novel vertical axis Darrieus turbine», *Energy*, vol. 89, pagg. 819–834, 2015, doi: 10.1016/j.energy.2015.05.136.

[10] J. Chen, P. Liu, H. Xu, L. Chen, M. Yang, e L. Yang, «A detailed investigation of a novel vertical axis Darrieus wind rotor with two sets of blades», *J. Renewable Sustainable Energy*, vol. 9, n. 1, 2017, doi: 10.1063/1.4977004.

[11] F. Arpino, M. Scungio, e G. Cortellessa, «Numerical performance assessment of an innovative Darrieus-style vertical axis wind turbine with auxiliary straight blades», *Energy Convers. Manage.*, vol. 171, pagg. 769–777, 2018, doi: 10.1016/j.enconman.2018.06.028.

[12] G. Fleit e S. Baranya, «An improved particle image velocimetry method for efficient flow analyses», *Flow. Meas. Instrum.*, vol. 69, 2019, doi: 10.1016/j.flowmeasinst.2019.101619.

[13] S. Yayla e S. Teksin, «Flow measurement around a cylindrical body by attaching flexible plate: A PIV approach», *Flow. Meas. Instrum.*, vol. 62, pagg. 56–65, 2018, doi: 10.1016/j.flowmeasinst.2018.05.003.
[14] S. Yagmur, S. Dogan, M. H. Aksoy, I. Goktepeli, e M. Ozgoren, «Comparison of flow characteristics around an equilateral triangular cylinder via PIV and Large Eddy Simulation methods», *Flow. Meas. Instrum.*, vol. 55, pagg. 23–36, 2017, doi: 10.1016/j.flowmeasinst.2017.04.001.
[15] D. Castelein, D. Ragni, G. Tescione, C. J. Simão Ferreira, e M. Gaunaa, «Creating a benchmark of vertical axis wind turbines in dynamic stall for validating numerical models», presentato al 33rd Wind Energy Symposium, 2015, [Online]. Disponibile su: https://www2.scopus.com/inward/record.uri?eid=2-s2.0-84937688429&partnerID=40&md5=7e4a0c41f7fe81a9ba0806343cde8ceb.
[16] J. M. Edwards, L. A. Danao, e R. J. Howell, «PIV measurements and CFD simulation of the performance and flow physics and of a small-scale vertical axis wind turbine», *Wind Energy*, vol. 18, n. 2, pagg. 201–217, 2015, doi: 10.1002/we.1690.
[17] A. Posa, C. M. Parker, M. C. Leftwich, e E. Balaras, «Wake structure of a single vertical axis wind turbine», *International Journal of Heat and Fluid Flow*, vol. 61, pagg. 75–84, 2016, doi: 10.1016/j.ijheatfluidflow.2016.02.002.
[18] H. F. Lam e H. Y. Peng, «Study of wake characteristics of a vertical axis wind turbine by two- and three-dimensional computational fluid dynamics simulations», *Renewable Energy*, vol. 90, pagg. 386–398, 2016, doi: 10.1016/j.renene.2016.01.011.
[19] M. Scungio, F. Arpino, V. Focanti, M. Profili, e M. Rotondi, «Wind tunnel testing of scaled models of a newly developed Darrieus-style vertical axis wind turbine with auxiliary straight blades», *Energy Convers. Manage.*, vol. 130, pagg. 60–70, 2016, doi: 10.1016/j.enconman.2016.10.033.
[20] M. Claessens, «The Design and Testing of Airfoils in Small Vertical Axis Wind Turbines», gen. 2006.
[21] R. D. Keane e R. J. Adrian, «Theory of cross-correlation analysis of PIV images», *Appl Sci Res (The Hague)*, vol. 49, n. 3, pagg. 191–215, 1992, doi: 10.1007/BF00384623.
[22] M. Stanislas e J. C. Monnier, «Practical aspects of image recording in particle image velocimetry», *Meas. Sci. Technol.*, vol. 8, n. 12, pagg. 1417–1426, 1997, doi: 10.1088/0957-0233/8/12/006.
[23] E. Lazar, B. DeBlauw, N. Glumac, C. Dutton, e G. Elliott, «A practical approach to PIV uncertainty analysis», presentato al 27th AIAA Aerodynamics Measurement and Ground Testing Conference, Chicago, IL, 2010, Consultato: giu. 28, 2010. [Online]. Disponibile su: https://www.scopus.com/inward/record.uri?eid=2-s2.0-84868611580&partnerID=40&md5=3ed671719fb506cfd218b470f073d7a3.
[24] M. Raffel, C. E. Willert, S. Wereley, e J. Kompenhans, *Particle Image Velocimetry. A Practical Guide*. Springer-Verlag Berlin Heidelberg, 2007.
[25] «ISO/IEC Guide 98-3:2008. Uncertainty of measurement - Part 3: Guide to the expression of uncertainty in measurement (GUM: 1995)», 2008.
[26] F. Arpino, N. Massarotti, A. Mauro, e L. Vanoli, «Metrological analysis of the measurement system for a micro-cogenerative SOFC module», *Int J Hydrogen Energy*, vol. 36, n. 16, pagg. 10228–10234, 2011, doi: 10.1016/j.ijhydene.2010.11.016.
[27] G. Ficco, M. Dell'Isola, P. Vigo, e L. Celenza, «Uncertainty analysis of energy measurements in natural gas transmission networks», *Flow. Meas. Instrum.*, vol. 42, pagg. 58–68, 2015, doi: 10.1016/j.flowmeasinst.2015.01.006.
[28] S. Niscio, «Uncertainty analysis: Particle imaging velocimetry (PIV).», 2008, vol. Section 75-01-03-03.

[29] F. Arpino, N. Massarotti, A. Mauro, e P. Nithiarasu, «Artificial compressibility-based CBS scheme for the solution of the generalized porous medium model», *Numer Heat Transfer Part B Fundam*, vol. 55, n. 3, pagg. 196–218, 2009, doi: 10.1080/10407790802628838.